

# Radiative ${}^3\text{He}(\alpha, \gamma){}^7\text{Be}$ reaction in Halo Effective Field Theory

Renato Higa <sup>a,\*</sup>, Gautam Rupak <sup>b,†</sup> and Akshay Vaghani <sup>b‡</sup>

<sup>a</sup> *Instituto de Física, Universidade de São Paulo,*

*R. do Matão 1371, 05508-090, São Paulo, SP, Brazil*

<sup>b</sup> *Department of Physics & Astronomy and HPC<sup>2</sup> Center for Computational Sciences,  
Mississippi State University, Mississippi State, MS 39762, U.S.A.*

## Abstract

In this work we study the radiative capture of  ${}^3\text{He}$  on  ${}^4\text{He}$  within the halo effective field theory (EFT) framework. At leading order the capture amplitude comprises the initial state  $s$ -wave strong and Coulomb interactions summed to all orders. At the same order in the expansion, leading two-body currents contribute as well. We find delicate cancelations between the various contributions, and the two-body current contributions can be replaced by appropriately enhancing the asymptotic normalizations of the  ${}^7\text{Be}$  ground and first excited state wave functions. The next-to-leading order corrections come from the  $s$ -wave shape parameter and the pure Coulomb  $d$ -wave initial state interactions. We fit the EFT parameters to available scattering data and most recent capture data. Our zero-energy astrophysical  $S$ -factor estimate,  $S_{34} \sim 0.55$  keV b, is consistent within error bars with the average in the literature.

PACS numbers: 25.40.Lw, 25.20.-x

Keywords: radiative capture, halo nuclei, effective field theory

---

\* higa@if.usp.br

† grupak@u.washington.edu

‡ av298@msstate.edu

## I. INTRODUCTION

Low-energy reaction rates involving light nuclei have become a recurrent subject nowadays, given their importance in many astrophysical processes. As astronomical observations aim at more accuracy, comparable improvements from experiments and theoretical estimates are desired for these reactions. An example is the process  ${}^3\text{He}(\alpha, \gamma){}^7\text{Be}$  that takes place in the interior of our Sun. The astrophysical  $S$ -factor for this reaction within the Gamov window  $E_G \sim 20$  keV is the main source of uncertainty in the solar neutrino flux detected on Earth. For instance, the flux of neutrinos from the  $\beta^+$  decay of  ${}^8\text{B}$  and from the electron capture on  ${}^7\text{Be}$  are proportional to  $[S_{34}]^{0.81}$  and  $[S_{34}]^{0.86}$ , respectively [1–3]. The first weak decay provides energetic solar neutrinos that were detected by Super-K [4] and SNO [5] but depends also on the  ${}^7\text{Be}(p, \gamma){}^8\text{B}$  reaction rate. Electron capture on  ${}^7\text{Be}$ , on the other hand, provides a solar neutrino flux three orders of magnitude higher than the former process [6, 7], with less energetic neutrinos which can be measured by the BOREXINO experiment at Gran Sasso [8], and depends exclusively on the  ${}^3\text{He}(\alpha, \gamma){}^7\text{Be}$  reaction. In either case, the need for a better description of the latter at very low energies is of prime importance in order to improve constraints from solar neutrinos, like mass hierarchy, flavor mixing angles and CP violating phases. Besides neutrino physics, the  ${}^3\text{He}(\alpha, \gamma){}^7\text{Be}(e^-, \nu){}^7\text{Li}$  chain reaction is the main source of  ${}^7\text{Li}$  production during big bang nucleosynthesis (BBN), with a Gamov window  $100 \text{ keV} \lesssim E_G \lesssim 900 \text{ keV}$ . The primordial abundance of  ${}^7\text{Li}$  calculated from BBN and WMAP cosmic baryon density measurements is a factor of 3 to 4 times larger than observations of metal-poor stars in our galaxy [1, 9, 10], which constitutes the so-called lithium problem. Many proposals to solve this puzzle, that involves alternative astronomical measurements and modeling, nuclear, and particle physics, can be strongly constrained with more reliable information on  $S_{34}$ , since the abundance ratio  ${}^7\text{Li}/\text{H} \propto [S_{34}]^{0.96}$  [1, 9].

Given its importance to the topics mentioned above, several measurements of the  ${}^3\text{He}(\alpha, \gamma){}^7\text{Be}$  reaction were done in the past (see [3] and references therein) and most recent years [1, 11]. As pointed out in Ref. [1], measurements done prior to the review article [3] fall into two discrepant groups—those based on induced  ${}^7\text{Be}$  activity, and those relying on prompt  $\gamma$ -ray detection. Due to improvements in detectors and background suppressions, this discrepancy is no longer present in the most recent measurements [11]. Nevertheless, error bars are still relatively large in the low-energy regime of astrophysical

interest, due to the strong suppression of events by the Coulomb repulsion. The higher energy data where statistics are better shall therefore be theoretically extrapolated down to astrophysically relevant energies in an as less model-dependent way as possible.

The  ${}^7\text{Be}$  nucleus has a predominant  ${}^3\text{He}\text{-}\alpha$  cluster structure. Its ground state binding energy,  $B_0 \sim 1.6$  MeV, is considerably smaller than the proton separation energy in  ${}^3\text{He}$  ( $S_p \sim 5.5$  MeV) and the energy of the first excited state of the  $\alpha$  particle ( $\sim 20$  MeV). The distinct two-cluster configuration of  ${}^7\text{Be}$ , with tight constituents and the low-energy regime one is interested in, make this reaction very suitable for a halo effective field theory (halo EFT) approach. Halo EFT was first formulated in Refs. [12, 13] in their study of the shallow  $p$ -wave neutron-alpha resonance and applied to other systems, such as the  $s$ -wave alpha-alpha resonance [14, 15], three-body halo nuclei [16, 17], coupled-channel proton- ${}^7\text{Li}$  scattering [18], electromagnetic transitions [19] and capture reactions [20–27]. In this work, we apply the same ideas to the  ${}^3\text{He}(\alpha, \gamma){}^7\text{Be}$  radiative reaction, following a two-cluster approach of point-like objects at leading order (LO) approximation. Corrections due to the structure of each cluster and higher order electromagnetic interactions are taken into account in perturbation theory. In halo EFT, a systematic and model-independent expansion of observables is achieved through the use of an expansion parameter —formed by the ratio of a soft momentum scale  $Q$ , associated with the shallowness of the binding of the clusters, and a hard momentum scale  $\Lambda$ , related to the tightness of the cores. Moreover, the formalism guarantees unambiguous inclusion of electromagnetic interactions that preserve the required symmetry constraints, such as gauge invariance.

The paper is organized as follows. In Sec. II we briefly comment on the energy scales, degrees of freedom, and channels relevant to the dominant E1 transition, as well as the construction of the corresponding interaction lagrangian. Sec. III presents the main elements necessary to deal with Coulomb interactions between the  ${}^3\text{He}$  and  $\alpha$  nuclei. The amplitude for both initial elastic scattering state and final bound state are obtained in the halo EFT framework in Sec. IV. There we also relate the EFT couplings to the effective range parameters and set the power-counting. Sec. V collects the relevant expressions for the capture amplitude and cross section, whose numerical results are shown and discussed in Sec. VI. We present the EFT power-counting here. Our concluding remarks are presented in Sec. VII.

## II. INTERACTION

The halo EFT we construct treats the  ${}^7\text{Be}$  nucleus as a bound state of point-like nuclear clusters  ${}^3\text{He}$  and  $\alpha$ . The  $\frac{3}{2}^-$  ground state has a binding energy  $B_0 = 1.5866$  MeV, and the  $\frac{1}{2}^-$  first excited state has a binding energy  $B_1 = 1.1575$  MeV. The next excited state of  ${}^7\text{Be}$  is about 3 MeV above the  ${}^3\text{He}$ - $\alpha$  threshold [28]. In halo EFT the ground and first excited states are included respectively as  ${}^2P_{3/2}$  and  ${}^2P_{1/2}$  in the spectroscopic notation  ${}^{2S+1}L_J$ . The states beyond the first excited state are not included in the low-energy theory. Similarly, only the ground states of  ${}^3\text{He}$  and  $\alpha$  are relevant at astrophysical energies.

Early works on radiative capture  ${}^3\text{He}(\alpha, \gamma){}^7\text{Be}$  indicate it is dominated by the E1 transition from the initial  $s$ -wave state at low energies, see Ref. [1]. In the phase shift analysis of experimental data we use, the Coulomb subtracted  $d$ -wave phase shift is found to be small and treated as zero [29]. In the EFT we include initial  $d$ -wave state with only Coulomb but no strong interaction. Thus we consider the following Lagrangian for the calculation,

$$\begin{aligned} \mathcal{L} = & \psi^\dagger \left[ i\partial_0 + \frac{\nabla^2}{2m_\psi} \right] \psi + \phi^\dagger \left[ i\partial_0 + \frac{\nabla^2}{2m_\phi} \right] \phi \\ & + \chi_{[j]}^{(\zeta)\dagger} \left[ \Delta^{(\zeta)} + i\partial_0 + \frac{\nabla^2}{2M} \right] \chi_{[j]}^{(\zeta)} + h^{(\zeta)} \left[ \chi_{[j]}^{(\zeta)\dagger} \psi P_{[j]}^{(\zeta)} \phi + \text{h. c.} \right], \end{aligned} \quad (1)$$

where the spin-1/2 fermion field  $\psi$  represents the  $\frac{1}{2}^+$   ${}^3\text{He}$  nucleus field with mass  $m_\psi = 2809.41$  MeV, and the scalar field  $\phi$  represents the spinless  $0^+$   $\alpha$  field, with mass  $m_\phi = 3728.4$  MeV.  $M = m_\psi + m_\phi$  is the total mass. We use natural units with  $\hbar = 1 = c$ . Note that, for some physical quantities, we keep more significant digits than necessary until presenting our final results. The projectors  $P_{[j]}$  and the auxiliary fields  $\chi_{[j]}^{(\zeta)}$  carry vector and spinor indices  $[j]$  to specify the relevant spin-angular momentum channels for the incoming states  $\zeta = {}^2S_{1/2}, {}^2D_{3/2}, {}^2D_{5/2}$ , final ground state  $\zeta = {}^2P_{3/2}$ , and final excited state  $\zeta = {}^2P_{1/2}$ , described below. We use the shorthand notation  $\zeta = \pm$  to refer to the  ${}^2P_{3/2}$  and  ${}^2P_{1/2}$  channels, respectively.

The  $s$ -wave interaction can be written using a spin-1/2 auxiliary field  $\chi^{\alpha,s}$  as:

$$\chi^{\alpha,s\dagger} \left[ \Delta^{(s)} + i\partial_0 + \frac{\nabla^2}{2M} \right] \chi^{\alpha,s} + h^{(s)} \left[ \chi^{\alpha,s\dagger} P^{\alpha\beta,s} \psi^\beta \phi + \text{h. c.} \right], \quad (2)$$

where the spinor indices  $\alpha, \beta$  on the fields  $\chi^{\alpha,s}$  and  $\psi^\beta$  are contracted using the diagonal  $s$ -wave projector  $P^{\alpha\beta,s} = \delta^{\alpha\beta}$ . The spinor index  $\alpha = 1, 2$ . The two  $s$ -wave couplings  $\Delta^{(s)}$

and  $h^{(s)}$  can be fitted to scattering length  $a_0$  and effective range  $r_0$  for elastic scattering of  ${}^3\text{He}$  and  $\alpha$ . We discuss this in more detail when we consider the relevant power-counting.

For the final state, we want to project the vector index  $i = 1, 2, 3$  for the  $p$ -wave and the spinor index  $\alpha$  for the  ${}^3\text{He}$  spin into total angular momentum  $j = 1/2$  and  $j = 3/2$  pieces. This can be done for a generic auxiliary field  $\chi_i^\alpha$  as follows:

$$\chi_i^\alpha = \frac{1}{3}(\sigma_i\sigma_j)^{\alpha\beta}\chi_j^\beta + \left[ \delta_{ij}\delta^{\alpha\beta} - \frac{1}{3}(\sigma_i\sigma_j)^{\alpha\beta} \right] \chi_j^\beta, \quad (3)$$

where the two pieces are the irreducible forms representing the  ${}^2P_{1/2}$  and  ${}^2P_{3/2}$  channels, respectively. The Pauli matrices  $\sigma_i$ 's act on the spinor indices. The two  $p$ -wave interactions can then be written as

$$\chi_i^{\alpha,\zeta\dagger} \left[ \Delta^{(\zeta)} + i\partial_0 + \frac{\nabla^2}{2M} \right] \chi_i^{\alpha,\zeta} + \sqrt{3}h^{(\zeta)} \left[ \chi_i^{\alpha,\zeta\dagger} P_{ij}^{\alpha\beta,\zeta} \psi^\beta \left( \frac{\vec{\nabla}}{m_\phi} - \frac{\overleftarrow{\nabla}}{m_\psi} \right)_j \phi + \text{h. c.} \right], \quad (4)$$

where the  $p$ -wave projectors are

$$\begin{aligned} P_{ij}^{\alpha\beta,\zeta} &= \frac{1}{3}(\sigma_i\sigma_j)^{\alpha\beta} & \text{for } \zeta = {}^2P_{1/2}, \\ P_{ij}^{\alpha\beta,\zeta} &= \delta_{ij}\delta^{\alpha\beta} - \frac{1}{3}(\sigma_i\sigma_j)^{\alpha\beta} & \text{for } \zeta = {}^2P_{3/2}. \end{aligned} \quad (5)$$

The two couplings  $\Delta^{(\zeta)}$ ,  $h^{(\zeta)}$  in each of the two  $p$ -wave channels can be determined from the corresponding binding momentum and effective range. For bound states, both of these couplings contribute at LO [12, 13]. This remains true even in the presence of long-range Coulomb interaction as we have here.

The capture calculation proceeds through the E1 transition. For one-body currents we couple the external photon through minimal substitution, that corresponds to gauging the momentum of the charged particle,  $\mathbf{p} \rightarrow \mathbf{p} + Ze\mathbf{A}$ , where  $Z$  is the charge number. We include the long-range Coulomb interaction between the  ${}^3\text{He}$  and  $\alpha$  nuclei to all orders in perturbation by summing the Coulomb ladder as described below. Two-body currents that are not related to elastic scattering operators by gauge invariance also contribute to the E1 transition between  $s$ -wave, and  $p$ -wave ground and excited states. These can be written using the auxiliary fields as

$$e\mu \left( \frac{Z_\phi}{m_\phi} - \frac{Z_\psi}{m_\psi} \right) L_{\text{E1}}^{(\zeta)} \sqrt{3}h^{(s)}h^{(\zeta)} \chi_i^{\alpha,\zeta\dagger} P_{ij}^{\alpha\beta,\zeta} \chi^{\beta,s} E_j, \quad (6)$$

where  $\mu$  is the reduced mass,  $\mathbf{E}$  is the electric field,  $Z_\psi = 2$  and  $Z_\phi = 2$  are the charge numbers of  ${}^3\text{He}$  and  $\alpha$ , respectively. We include factors of  $h^{(s)}$ ,  $h^{(\zeta)}$  and the effective charge

$e\mu(Z_\phi/m_\phi - Z_\psi/m_\psi)$  in the definition of the coupling  $L_{E1}$ . In the absence of Coulomb interaction, for a single charged particle, this reduces to a factor of  $\sim 2\pi/(\mu\sqrt{r_0 r_1^{(c)}})$  that has been suggested earlier [30]. Two-body currents such as this are usually not included in potential model calculations. Note that in our halo EFT formalism the one- and two-body currents are effective ones, whose origins lie in a more complicated one- and many-nucleon electromagnetic currents. The intricate contributions between different many-nucleon currents are discussed in a variational 4-nucleon study of Refs. [31, 32] and in a three-cluster ( $p$ - $d$ - $^4\text{He}$ ) model of Ref. [33], but is beyond the scope of this work.

### III. COULOMB LADDER

For the scattering of two charged particles  $^3\text{He}$  and  $\alpha$  at low energy, the relevant quantity that provides the strength of Coulomb photon exchanges is the Sommerfeld parameter  $\eta_p = \alpha_e Z_\psi Z_\phi \mu / p$ , where  $\alpha_e = e^2/(4\pi) \approx 1/137$  is the electromagnetic fine structure constant, and  $p$  is the relative center-of-mass (c.m.) momentum. The inverse of the Bohr radius of the system defines the momentum scale  $k_C = \alpha_e Z_\psi Z_\phi \mu$  and the Sommerfeld parameter is written as the ratio  $\eta_p = k_C/p$ . Each photon exchange is proportional to  $\eta_p$ . In the low-energy region that we consider,  $p \lesssim k_C$ , multiple photon exchanges contribute at least at the same order, forcing the summation of Coulomb ladder diagrams, Fig. 1.

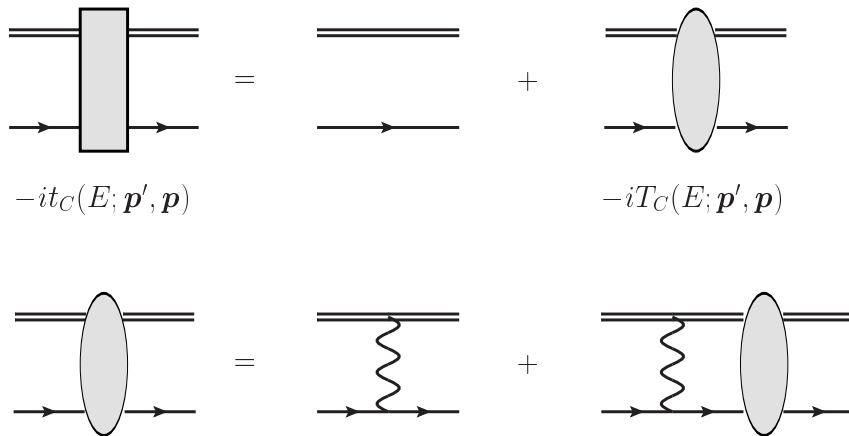


FIG. 1. Coulomb ladder diagrams. The double line represents the scalar  $\alpha$  particle, and the single line with an arrow the fermionic  $^3\text{He}$  nucleus. The wavy lines represent photons. We only include Coulomb photon interaction between the charged particles.

The Coulomb scattering amplitude  $T_C$  satisfies the following useful relations

$$\begin{aligned} |\chi_p^{(\pm)}\rangle &= |\mathbf{p}\rangle + \widehat{G}_0^{(\pm)} \widehat{T}_C |\mathbf{p}\rangle, \\ \widehat{G}_C^{(\pm)} &= \widehat{G}_0^{(\pm)} + \widehat{G}_0^{(\pm)} \widehat{T}_C \widehat{G}_0^{(\pm)}, \end{aligned} \quad (7)$$

where  $|\mathbf{p}\rangle$  is a plane wave state in the two-particle c.m. system, and  $|\chi_k^{(+)}\rangle$  ( $|\chi_k^{(-)}\rangle$ ) is the incoming (outgoing) Coulomb scattering state. The free and Coulomb Green's functions as operators are respectively written as

$$\begin{aligned} \widehat{G}_0^{(\pm)} &= (E - \widehat{H}_0 \pm i\epsilon)^{-1}, \\ \widehat{G}_C^{(\pm)} &= (E - \widehat{H}_0 - \widehat{V}_C \pm i\epsilon)^{-1}. \end{aligned} \quad (8)$$

The  $\pm i\epsilon$  signs in the definitions correspond to retarded and advanced Green's functions. Taking expectation values between final  $\langle \mathbf{p}' |$  and initial  $|\mathbf{p}\rangle$  momentum states, one can derive several useful relations,

$$\begin{aligned} G_0^{(\pm)}(E; \mathbf{p}', \mathbf{p}) &\equiv \langle \mathbf{p}' | \widehat{G}_0^{(\pm)} | \mathbf{p} \rangle = \frac{(2\pi)^3 \delta(\mathbf{p}' - \mathbf{p})}{E - p'^2/(2\mu) \pm i\epsilon}, \\ \frac{T_C(E; \mathbf{p}', \mathbf{p})}{E - p'^2/(2\mu) \pm i\epsilon} &\equiv \langle \mathbf{p}' | \widehat{G}_0 \widehat{T}_C | \mathbf{p} \rangle = \chi_p^{(\pm)}(\mathbf{p}') - (2\pi)^3 \delta(\mathbf{p}' - \mathbf{p}), \\ G_C^{(\pm)}(E; \mathbf{p}', \mathbf{p}) &\equiv \langle \mathbf{p}' | \widehat{G}_C^{(\pm)} | \mathbf{p} \rangle \\ &= G_0^{(\pm)}(E; \mathbf{p}', \mathbf{p}) + \frac{T_C(E; \mathbf{p}', \mathbf{p})}{[E - p'^2/(2\mu) \pm i\epsilon] [E - p^2/(2\mu) \pm i\epsilon]}, \end{aligned} \quad (9)$$

with  $\chi_p^{(\pm)}(\mathbf{p}') \equiv \langle \mathbf{p}' | \chi_p^{(\pm)} \rangle$ . The diagrammatic relation between  $\widehat{t}_C$  and  $\widehat{T}_C$  from Fig. 1 can be expressed as

$$t_C(E; \mathbf{p}', \mathbf{p}) = (2\pi)^3 \delta(\mathbf{p}' - \mathbf{p}) \left( E - \frac{p'^2}{2\mu} \pm i\epsilon \right) + T_C(E; \mathbf{p}', \mathbf{p}), \quad (10)$$

and helps write  $t_C(E; \mathbf{p}', \mathbf{p})$  in terms of  $\chi_p^{(\pm)}(\mathbf{p}')$  and  $G_C^{(\pm)}(E; \mathbf{p}', \mathbf{p})$ .

The Coulomb wave function and the retarded Green's function are known in closed form in coordinate space [34, 35],

$$\begin{aligned} \tilde{\chi}_p^{(\pm)}(\mathbf{r}) &\equiv e^{-\frac{\eta_p \pi}{2}} \Gamma(1 \pm i\eta_p) {}_1F_1(\mp i\eta_p, 1; \pm ipr - i\mathbf{p} \cdot \mathbf{r}) e^{i\mathbf{p} \cdot \mathbf{r}}, \\ \tilde{\chi}_p^{(+)}(\mathbf{r}) &= \sum_{l=0}^{\infty} (2l+1) i^l e^{i\sigma_l} P_l(\hat{\mathbf{p}} \cdot \hat{\mathbf{r}}) \frac{F_l(\eta_p, pr)}{pr}, \\ G_C^{(+)}(E; \mathbf{r}', \mathbf{r}) &\equiv \sum_{l=0}^{\infty} (2l+1) P_l(\hat{\mathbf{r}}' \cdot \hat{\mathbf{r}}) G_C^{(l)}(E, r', r), \\ G_C^{(l)}(E, r', r) &= -\frac{\mu p}{2\pi} \frac{F_l(\eta_p, r_{<p})}{r_{<p}} \frac{H_l^{(+)}(\eta_p, r_{>p})}{r_{>p}}, \end{aligned} \quad (11)$$

where  $r_<$  ( $r_>$ ) correspond to the lesser (greater) of the coordinates  $r$ ,  $r'$ , and

$$\begin{aligned} F_l(\eta_p, \rho) &= C_l(\eta_p) 2^{-l-1} (-i)^{l+1} M_{i\eta_p, l+1/2}(2i\rho), \\ H_l^{(+)}(\eta_p, \rho) &= (-i)^l e^{\pi\eta_p/2} e^{i\sigma_l(\eta_p)} W_{-i\eta_p, l+1/2}(-i2\rho), \\ C_l(\eta_p) &= \frac{2^l e^{-\pi\eta_p/2} |\Gamma(l+1+i\eta_p)|}{\Gamma(2l+2)}, \end{aligned} \quad (12)$$

with conventionally defined Whittaker functions  $M_{k,\mu}(z)$  and  $W_{k,\mu}(z)$ .  $F_l(\eta_p, \rho)$  is the regular Coulomb wave function, the irregular wave function is given by  $G_l(\eta_p, \rho) = H_l^{(+)}(\eta_p, \rho) - iF_l(\eta_p, \rho)$ , and  $\sigma_l = \arg \Gamma(l+1+i\eta_p)$  is the Coulomb phase shift. We define the Coulomb Green's function for a bound state with binding energy  $B$  as

$$G_C^{(l)}(-B, r', r) = -i \frac{\mu\gamma}{2\pi} \frac{F_l(\eta_{i\gamma}, i\gamma r')}{i\gamma r'} \frac{H_l^{(+)}(\eta_{i\gamma}, i\gamma r)}{i\gamma r}, \quad (13)$$

where  $\gamma = \sqrt{2\mu B}$  is the binding momentum. The coordinate space definitions assume  $r' < r$ . In the limit  $r' \sim 0 \ll r \sim \infty$  for charged neutral particles ( $Z_\psi = 0 = Z_\phi$ ), we recover the expected result

$$G_C^{(0)}(-B, r' \rightarrow 0, r) \sim -\frac{\mu}{2\pi r} e^{-\gamma r}. \quad (14)$$

#### IV. ELASTIC SCATTERING

The elastic scattering amplitude  $T(E; \mathbf{p}', \mathbf{p})$  in the presence of both short-range strong and long-range Coulomb interactions is traditionally written as

$$T(E; \mathbf{p}', \mathbf{p}) = T_C(E; \mathbf{p}', \mathbf{p}) + T_{SC}(E; \mathbf{p}', \mathbf{p}), \quad (15)$$

where the purely Coulomb contribution can be written as

$$T_C(E; \mathbf{p}', \mathbf{p}) = \sum_{l=0}^{\infty} (2l+1) T_C^{(l)}(E; p) P_l(\hat{\mathbf{p}}' \cdot \hat{\mathbf{p}}) = -\frac{2\pi}{\mu} \sum_{l=0}^{\infty} (2l+1) \frac{e^{2i\sigma_l} - 1}{2ip} P_l(\hat{\mathbf{p}}' \cdot \hat{\mathbf{p}}), \quad (16)$$

using the incoming (outgoing) c.m. momentum  $\mathbf{p}$  ( $\mathbf{p}'$ ).

The on-shell Coulomb-subtracted amplitude can also be expanded in partial waves as

$$T_{SC}^{(l)} = -\frac{2\pi}{\mu} \frac{e^{2i\sigma_l}}{p \cot \delta_l - ip}, \quad (17)$$

where the full phase shift is simply  $\delta_l + \sigma_l$ . The Coulomb-subtracted phase shift  $\delta_l$  is usually expressed in terms of a modified effective range expansion (ERE)

$$\left[ \frac{\Gamma(2l+2)}{2^l \Gamma(l+1)} \right]^2 [C_l(\eta_p)]^2 p^{2l+1} (\cot \delta_l - i) = -\frac{1}{a_l} + \frac{1}{2} r_l p^2 + \frac{1}{4} s_l p^4 + \dots$$

$$-\frac{2k_C p^{2l}}{\Gamma(l+1)^2} \frac{|\Gamma(l+1+i\eta_p)|^2}{|\Gamma(1+i\eta_p)|^2} H(\eta_p),$$

$$H(\eta) = \psi(i\eta) + \frac{1}{2i\eta} - \ln(i\eta), \quad (18)$$

with  $\psi(x)$  the digamma function. The  $\dots$  above represents terms with higher powers in  $p^2$ .

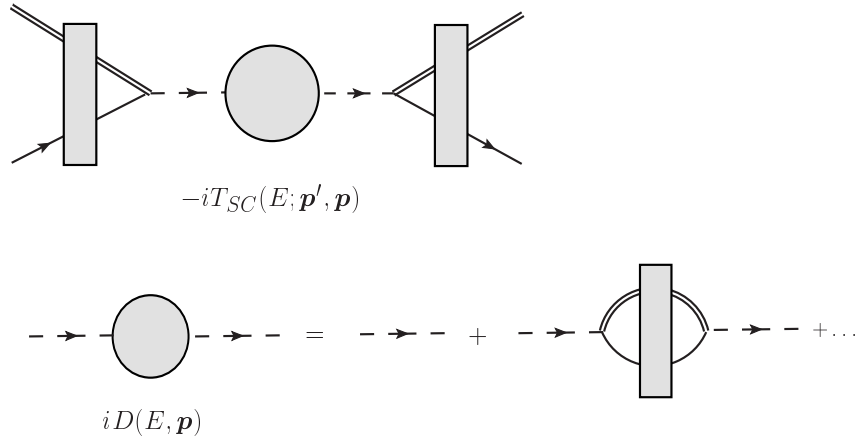


FIG. 2. Elastic scattering in  $s$ - and  $p$ -wave. The dashed line represents the auxiliary field  $\chi$  in  $s$ - and  $p$ -wave as appropriate. The rest of the notation is the same as in Fig. 1.

The amplitude  $T_{SC}$  is given in EFT by the set of diagrams in Fig. 2. The  $s$ -wave amplitude for c.m. incoming momentum  $\mathbf{p}$  and outgoing momentum  $\mathbf{p}'$ , with  $p = |\mathbf{p}| = |\mathbf{p}'|$  and  $E = p^2/(2\mu)$ , can be written as

$$-iT_{SC}^{(0)} = (2\mu)^2 \left[ \int \frac{d^3k}{(2\pi)^3} \frac{t_c(E; \mathbf{p}', \mathbf{k})}{k^2 - p^2 - i\epsilon} \right] [-i(h^{(s)})^2 D^{(s)}(E, 0)] \left[ \int \frac{d^3l}{(2\pi)^3} \frac{t_c(E; \mathbf{l}, \mathbf{p})}{l^2 - p^2 - i\epsilon} \right]$$

$$= -i[h^{(s)}]^2 D^{(s)}(E, 0) \tilde{\chi}_{p'}^{(-)*}(0) \tilde{\chi}_p^{(+)}(0) = -i[h^{(s)}]^2 D^{(s)}(E, 0) C_0^2(\eta_p) e^{i2\sigma_0}, \quad (19)$$

where the dressed dimer propagator is given by

$$D^{(s)}(p_0, \mathbf{p} = 0) = \frac{1}{\Delta^{(s)} + p_0 - [h^{(s)}]^2 J_0(\sqrt{2\mu p_0})},$$

$$J_0(p = \sqrt{2\mu E}) = G_C(E; r = 0, r' = 0) = -2\mu \int \frac{d^3q}{(2\pi)^3} \frac{1}{[q^2 - p^2 - i\epsilon]} \frac{2\pi\eta_q}{[e^{2\pi\eta_q} - 1]}. \quad (20)$$

Using the modified ERE from Eq. (18) in Eq. (17) and comparing to the  $s$ -wave EFT expression in Eq. (19), we can determine the two couplings in terms of  $a_0$  and  $r_0$ ,

$$\begin{aligned}\Delta^{(s)} &= \frac{\mu h^{(s)2}}{2\pi a_0} - \frac{\mu h^{(s)2}}{2\pi} \left\{ 2k_C \left[ \frac{1}{D-4} - \ln \left( \frac{\lambda\sqrt{\pi}}{2k_C} \right) - 1 + \frac{3}{2}C_E \right] + \lambda \right\}, \\ [h^{(s)}]^2 &= -\frac{2\pi}{\mu^2 r_0},\end{aligned}\quad (21)$$

where the space-time dimensions  $D \rightarrow 4$  and  $\lambda$  is the renormalization scale within the power-divergence subtraction (PDS) scheme [36]. The  $\lambda$ -dependent EFT couplings were derived to reproduce the scattering amplitude written only in terms of scattering parameters  $a_0$ ,  $r_0$ , etc. Thus the physical observables are finite and explicitly independent of  $\lambda$ .

The elastic scattering amplitude requires non-perturbative treatment of the Coulomb photons at low energies. However, it is not clear if the short-range interaction contained in the parameters  $a_0$ ,  $r_0$ , etc., should be included in perturbation or not. Fitting the EFT expression to both elastic and capture data *a posteriori*, we find that both the scattering length  $a_0$  and the effective range  $r_0$  contribute at LO. We propose a power-counting where  $a_0 \sim \Lambda^2/Q^3$  is fine-tuned, and  $r_0 \sim 1/\Lambda$  is of natural size. However, there is a further fine-tuning in that the combination  $r_0 p^2/2 - 2k_C H(\eta_p) \sim Q^3/\Lambda^2$  for low momentum  $p \sim Q$  [14]. Then the  $s$ -wave scattering amplitude gets LO contributions from  $a_0$ ,  $r_0$  for  $p \sim Q$ . The contribution from a natural-size shape parameter  $s_0 \sim 1/\Lambda^3$  is suppressed by a relative factor of  $Q/\Lambda$ , and contributes at NLO.

The  $p$ -wave amplitude is written as

$$-i3T_{SC}^{(1)}\hat{\mathbf{p}}' \cdot \hat{\mathbf{p}} = -i[h^{(\zeta)}]^2 D^{(\zeta)}(E, 0)[\nabla_a \tilde{\chi}_{p'}^{(-)*}(0)][\nabla_a \tilde{\chi}_p^{(+)}(0)], \quad (22)$$

with the  $p$ -wave dressed dimer propagator written as

$$\begin{aligned}D^{(\zeta)}(E, 0) &= \frac{1}{\Delta^{(\zeta)} + E - 3[h^{(\zeta)}]^2 J_1(p)/\mu^2}, \\ J_1(p) &= -\frac{2\mu}{n} \int \frac{d^n k}{(2\pi)^n} \frac{1}{k^2 - p^2 - i\delta} [\nabla_a \tilde{\chi}_k^{(+)*}(0)][\nabla_a \tilde{\chi}_k^{(+)}(0)].\end{aligned}\quad (23)$$

$J_1(p)$  is given by a divergent integral that we regulate through dimensional regularization in  $n = D - 1$  space dimensions. Using the relations

$$\begin{aligned}[\nabla_a \tilde{\chi}_{p'}^{(-)*}(0)][\nabla_a \tilde{\chi}_p^{(+)}(0)] &= e^{-\pi\eta_p} \Gamma(2 + i\eta_p)^2 \mathbf{p}' \cdot \mathbf{p}, \\ [\nabla_a \tilde{\chi}_k^{(+)*}(0)][\nabla_a \tilde{\chi}_k^{(+)}(0)] &= (k^2 + \beta^2) \frac{2\pi\eta_k}{e^{2\pi\eta_k} - 1},\end{aligned}\quad (24)$$

the PDS prescription for the integrals, and relating Eqs. (17), (18) to Eq. (22), one gets

$$\begin{aligned}\Delta^{(\zeta)} &= \frac{h^{(\zeta)2}}{2\pi\mu a_1} - \frac{h^{(\zeta)2}}{2\pi\mu} \left\{ 2k_C^3 \left[ \frac{1}{D-4} - \ln \left( \frac{\lambda\sqrt{\pi}}{2k_C} \right) - 1 + \frac{3}{2}C_E \right] \right. \\ &\quad \left. + k_C^2 \left( \frac{3\lambda}{2} - \frac{2k_C}{3} \right) + 8\pi^2 k_C^3 \zeta'(-2) + \frac{\pi^2 \lambda k_C^2}{2} - \frac{3\pi \lambda^2 k_C}{2} + \frac{\pi \lambda^3}{2} \right\}, \\ \frac{2\pi}{[h^{(\zeta)}]^2} &= -r_1^{(\zeta)} - 2 \left\{ 2k_C \left[ \frac{1}{D-4} - \ln \left( \frac{\lambda\sqrt{\pi}}{2k_C} \right) - 1 + \frac{3}{2}C_E \right] + \left( \frac{3\lambda}{2} - \frac{2k_C}{3} \right) \right\}.\end{aligned}\quad (25)$$

The  $p$ -wave amplitude is  $\lambda$ -independent though the EFT couplings evolve as functions of it, similar to the  $s$ -wave result above.

The dressed  $p$ -wave dimer propagator defines the wave function renormalization constant

$$\begin{aligned}\frac{1}{\mathcal{Z}^{(\zeta)}} &= \frac{\partial}{\partial p_0} [D^{(\zeta)}(p_0; \mathbf{p})^{-1}] \Big|_{p_0=p^2/(2\mu)-B^{(\zeta)}} \\ &= -\frac{h^{(\zeta)2}}{2\pi p} \frac{\partial}{\partial p} \left[ -\frac{1}{a_1} + \frac{1}{2}r_1 p^2 + \frac{1}{4}s_1 + \dots - 2k_C(k_C^2 + p^2)H(\eta_p) \right] \Big|_{p=i\gamma},\end{aligned}\quad (26)$$

where  $B^{(\zeta)}$  is the  $p$ -wave binding energy. To ensure the modified ERE parameters are consistent with the bound state energies we redefine the ERE for  $p$ -waves as

$$\begin{aligned}9[C_1(\eta_p)]^2 p^3 (\cot \delta_1 - i) &= 2k_C(k_C^2 - \gamma^2)H(-i\eta_\gamma) + \frac{1}{2}\rho_1(p^2 + \gamma^2) + \frac{1}{4}\sigma_1(p^2 + \gamma^2)^2 + \dots \\ &\quad - 2k_C(k_C^2 + p^2)H(\eta_p).\end{aligned}\quad (27)$$

A straightforward calculation leads to

$$-\frac{2\pi}{h^{(\zeta)2}\mathcal{Z}^{(\zeta)}} = \rho_1^{(\zeta)} - 4k_C H\left(-i\frac{k_C}{\gamma}\right) - \frac{2k_C^2}{\gamma^3}(k_C^2 - \gamma^2) \left[ \psi'\left(\frac{k_C}{\gamma}\right) - \frac{\gamma^2}{2k_C^2} - \frac{\gamma}{k_C} \right],\quad (28)$$

such that the wave function renormalization constant depends only on the binding momentum  $\gamma$  and the effective range  $\rho_1$ , to all orders in perturbation. From the second relation in Eq. (25), we propose  $\frac{2\pi}{[h^{(\zeta)}]^2} \sim Q \sim k_C \sim r_1^{(\zeta)} \sim \rho_1^{(\zeta)}$ . Then the first relation gives  $\Delta^{(\zeta)} \sim Q^2/\mu$ , and all the terms in the denominator of the dimer propagator in Eq. (23) scale as  $Q^2/\mu$ . This makes the contribution from the binding momentum  $\gamma$  and effective range  $\rho_1$  LO. The combination  $h^{(\zeta)2}\mathcal{Z}^{(\zeta)}$  controls the normalization of the capture cross-section as shown in the next section. The shape parameter  $\sigma_1$  does not contribute to the wave function renormalization or the capture cross section. However, a natural-size  $\sigma_1 \sim 1/\Lambda$  would contribute to the  $p$ -wave phase shift at NLO.

## V. RADIATIVE CAPTURE

We assign the c.m. momenta  $\mathbf{p}$  to the  $\alpha$  particle, and  $\mathbf{k}$  to the outgoing photon in the final state. From energy-momentum conservation  $|\mathbf{k}| = (p^2 + \gamma^2)/(2\mu) \sim Q^2/\mu \ll Q \sim \gamma \sim p$  in the EFT power-counting. Thus in a typical loop calculation a combination such as  $E_\psi + k_0 + q_0 - (\mathbf{q} + \mathbf{k} + \mathbf{p})^2/(2m_\psi)$  is approximated as  $E_\psi + k_0 + q_0 - (\mathbf{q} + \mathbf{p})^2/(2m_\psi) \sim Q^2/\mu$  where  $E_\psi = p^2/(2m_\psi)$  and  $(q_0, \mathbf{q})$  is the loop energy-momentum. This approximation corresponds to zero-recoil of the final bound state  ${}^7\text{Be}$ . We count  $Q/\mu \sim Q^2/\Lambda^2 \ll Q/\Lambda$  and neglect recoil effects in this calculation up to NLO.

In this section we present some of the Feynman diagrams that contribute to the capture process, see Figs. 3, 4, 5. In the next section when we present our analysis, we elaborate more on the power-counting and discuss how these sets of diagrams constitute the EFT contribution up to NLO. We consider E1 transitions from the initial  ${}^2S_{1/2}$  state to both final bound states, ground  ${}^2P_{3/2}$  and excited  ${}^2P_{1/2}$ . The external photon is minimally coupled to the charged clusters at LO. Capture from initial  ${}^2D_{5/2}$  and  ${}^2D_{3/2}$  states without strong interaction are included as well.

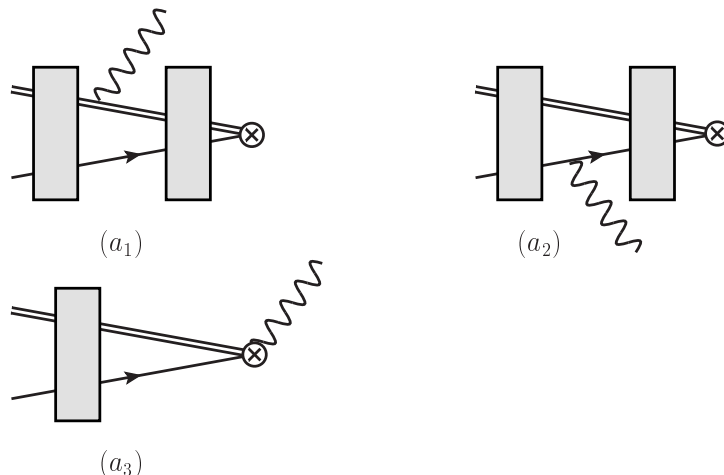


FIG. 3. Group A diagrams. Radiative capture without initial state strong interaction. The  $\otimes$  represents the final bound state. The external photon represented by the wavy line is minimally coupled to the charged particles as described in the text. The rest of the notation is the same as in Figs 1, 2.

The first set of diagrams from Fig. 3 include only Coulomb interactions for the incoming

charged particles  ${}^3\text{He}$  and  $\alpha$ . We find for  $s$ -wave capture

$$\begin{aligned}
(a_1) + (a_2) &= -\frac{e^{i\sigma_0} A(p)}{\mu} C_0(\eta_p) \Gamma_{aa}^{(\zeta)}, \\
(a_3) &= -\tilde{\chi}_p^{(+)}(\mathbf{r} = \mathbf{0}) \Gamma_{aa}^{(\zeta)} = -C_0(\eta_p) e^{i\sigma_0} \Gamma_{aa}^{(\zeta)}, \\
A(p) &= \frac{2\gamma\mu}{3} \frac{\Gamma(2 + k_C/\gamma)}{C_0(\eta_p)} \int_0^\infty dr r W_{-k_C/\gamma, 3/2}(2\gamma r) \partial_r \left[ \frac{F_0(k_C/p)}{pr} \right], \quad (29)
\end{aligned}$$

where the index  $\zeta$  refers to the final  $p$ -wave bound states. The corresponding binding momentum  $\gamma$  is given by  $\gamma_0 = \sqrt{2\mu B_0}$  and  $\gamma_1 = \sqrt{2\mu B_1}$  for the ground and the first excited states, respectively. The Whittaker function  $W_{-k_C/\gamma, 3/2}(2\gamma r)$  is associated with the final  $p$ -wave bound state, and the  $s$ -wave Coulomb wave function  $F_0(\eta_p)$  is associated with the initial incoming scattering state. There is also a  $d$ -wave contribution from diagrams  $(a_1) + (a_2)$  that is given by

$$\begin{aligned}
&-3\mu e^{i\sigma_2} Y(p) (\hat{p}_a \hat{p}_b - \frac{1}{3} \delta_{ab}) \Gamma_{ab}, \quad \text{with} \\
Y(p) &= \frac{2\gamma}{3} \Gamma(2 + k_C/\gamma) \int_0^\infty dr r W_{-k_C/\gamma, 3/2}(2\gamma r) \left( \frac{\partial}{\partial r} + \frac{3}{r} \right) \frac{F_2(\eta_p, rp)}{rp}, \quad (30)
\end{aligned}$$

where we chose the incoming relative momentum  $\mathbf{p}$  to point in the  $\hat{z}$ -direction.

The projection onto the  $p$ -wave states is given by

$$\Gamma_{ab}^{(\zeta)} = \left( \frac{eZ_\phi}{m_\phi} - \frac{eZ_\psi}{m_\psi} \right) (h^{(\zeta)} \sqrt{3} \sqrt{\mathcal{Z}^{(\zeta)}} \sqrt{2m_\phi}) \epsilon_a^* U_i^{*\alpha, \zeta}(-\vec{\mathbf{k}}) P_{ib}^{\alpha\beta, \zeta} U^{\beta, \psi}(-\vec{\mathbf{p}}), \quad (31)$$

where  $\epsilon_a$  is the photon polarization vector,  $\mathcal{Z}^{(\zeta)}$  is given by Eq. (28),  $U^\zeta$  is the spinor field for the  $p$ -wave final state with mass  $M = m_\psi + m_\phi$ , and  $U^\psi$  is the spinor field for the incoming  ${}^3\text{He}$  nucleus. The spinor fields satisfy the completeness relations

$$\begin{aligned}
\sum_{\text{pol.}} U_i^{\alpha, \zeta}(\mathbf{p}) [U_j^{\beta, \zeta}(\mathbf{p})]^* &= 2M P_{ij}^{\alpha\beta, \zeta}, \\
\sum_{\text{pol.}} U^{\alpha, \psi}(\mathbf{p}) [U^{\beta, \psi}(\mathbf{p})]^* &= 2m_\psi \delta^{\alpha\beta}, \quad (32)
\end{aligned}$$

where  $i, j$  are vector indices, and  $\alpha, \beta$  are spin indices.

The second set of diagrams from Fig. 4 involve the initial state short-range interaction

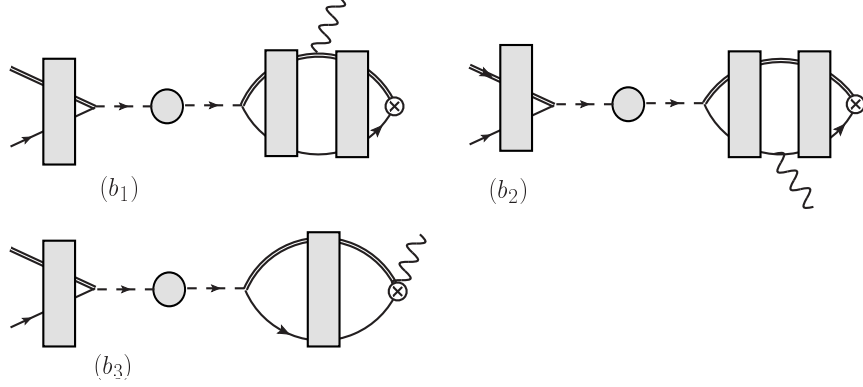


FIG. 4. Group B diagrams. Radiative capture with initial state  $s$ -wave strong interaction represented by the dressed dimer. We use the same notation as Figs. 1, 2 and 3.

that is constrained by the  $s$ -wave phase shift through the ERE. We find

$$\begin{aligned}
(b_1) + (b_2) &= \frac{2\pi}{\mu - \frac{1}{a_0} + \frac{r_0}{2}p^2 + \frac{s_0}{4}p^4 + \dots - 2k_C H(\eta_p)} \frac{C_0(\eta_p) e^{i\sigma_0}}{\mu} \frac{B_{ab}(p)}{\mu} \Gamma_{ab}, \\
B_{ab}(p) &= -3 \int d^3r \left[ \frac{G_C^{(1)}(-B; r', r)}{r'} \right] \Big|_{r'=0} \frac{\partial G_C^{(+)}(E; \mathbf{r}, 0)}{\partial r_a} \frac{r_b}{r}, \\
\left[ \frac{G_C^{(1)}(-B; r', r)}{r'} \right] \Big|_{r'=0} &= -\frac{\mu\gamma}{6\pi r} \Gamma(2 + k_C/\gamma) W_{-k_C/\gamma, 3/2}(2\gamma r), \\
G_C^{(+)}(E; \mathbf{r}, 0) &= -\frac{\mu}{2\pi r} \Gamma(1 + ik_C/p) W_{-ik_C/p, 1/2}(-i2pr). \tag{33}
\end{aligned}$$

The integral  $B_{ab}$  is divergent, which is rendered finite when combined with the contribution from the third diagram,

$$(b_3) = \frac{2\pi}{\mu - \frac{1}{a_0} + \frac{r_0}{2}p^2 + \frac{s_0}{4}p^4 + \dots - 2k_C H(\eta_p)} \frac{C_0(\eta_p) e^{i\sigma_0}}{\mu} J_0(p) \Gamma_{aa}. \tag{34}$$

We regulate the divergences using PDS, which is most conveniently done in this calculation in momentum space. The divergences come from zero and single Coulomb photon exchanges. Thus we analytically calculate the divergent pieces perturbatively up to  $\mathcal{O}(\alpha_e)$  and calculate

the rest (more than a single Coulomb photon), that is not divergent, numerically:

$$\begin{aligned}
B_{ab}(p) &\equiv B_{ab}^{(0)}(p) + \alpha_e B_{ab}^{(1)}(p) + \Delta B_{ab}(p), \\
B_{ab}^{(0)} &\equiv B^{(0)} \delta_{ab} = \mu^2 \left[ \frac{\lambda}{2\pi} + \frac{1}{3\pi} \frac{ip^3 - \gamma^3}{p^2 + \gamma^2} \right] \delta_{ab}, \\
\alpha_e B_{ab}^{(1)} &\equiv \alpha_e B^{(1)} \delta_{ab} = -\frac{k_C \mu^2}{2\pi} \left[ \frac{1}{4-D} + \ln \frac{\pi \lambda^2}{4k_C^2} - \gamma_E - \frac{2}{3} + \ln 4\pi \right] \delta_{ab} + k_C C(p) \delta_{ab}, \\
C(p) &= \frac{\mu^2}{6\pi^2(p^2 + \gamma^2)} \int_0^1 dx \int_0^1 dy \frac{1}{\sqrt{x(1-x)}\sqrt{1-y}} \\
&\times \left( xp^2 \ln \left[ \frac{\pi}{4k_C^2} (-yp^2 + (1-y)\gamma^2/x - i\delta) \right] \right. \\
&+ p^2 \ln \left[ \frac{\pi}{4k_C^2} (-yp^2 - (1-y)p^2/x - i\delta) \right] \\
&+ x\gamma^2 \ln \left[ \frac{\pi}{4k_C^2} (y\gamma^2 + (1-y)\gamma^2/x - i\delta) \right] \\
&\left. + \gamma^2 \ln \left[ \frac{\pi}{4k_C^2} (y\gamma^2 - (1-y)p^2/x - i\delta) \right] \right). \tag{35}
\end{aligned}$$

The double integral  $C(p)$  can be reduced further to a single integral that we evaluate numerically. The finite piece  $\Delta B_{ab}$  is evaluated numerically where we use spherical symmetry to write  $(r_b/r)[\partial/\partial r_a] = (r_a r_b/r^2)[\partial/\partial r] \rightarrow (\delta_{ab}/3)[\partial/\partial r]$  in the integral. Consequently,  $\Delta B_{ab}(p) \equiv \Delta B(p)\delta_{ab}$  and also  $B_{ab}(p) \equiv B(p)\delta_{ab}$ .

We do a similar decomposition of  $J_0(p)$  to write

$$\begin{aligned}
J_0(p) &= J_0^{(0)}(p) + \alpha_e J_0^{(1)} + \Delta J_0(p), \\
J_0^{(0)}(p) &= -\frac{\mu}{2\pi} (ip + \lambda), \\
\alpha_e J_0^{(1)} &= \frac{k_C \mu}{2\pi} \left[ \frac{1}{4-D} + 1 - \gamma_E + i\pi + \ln \frac{\pi \lambda^2}{4p^2} \right], \tag{36}
\end{aligned}$$

and the finite piece as

$$\begin{aligned}
\Delta J_0(0) &= -2\mu \int \frac{d^n q}{(2\pi)^n} \frac{1}{q^2 - p^2 - i\delta} \left[ \frac{2\pi\eta_q}{\exp(2\pi\eta_q) - 1} - 1 + \pi\eta_q \right] \\
&= \frac{i\mu p}{2\pi} + \frac{k_C \mu}{2\pi} \left[ -2H(\eta_p) - 2\gamma_E - i\pi + \ln \frac{p^2}{k_C^2} \right]. \tag{37}
\end{aligned}$$

Comparing Eqs. (35) and (36), we see that the divergent pieces in the term  $J_0(p) + B(p)/\mu$  cancel when combining diagrams  $(b_1) + (b_2)$  with  $(b_3)$ . The final result is finite and independent of the renormalization scale  $\lambda$ .

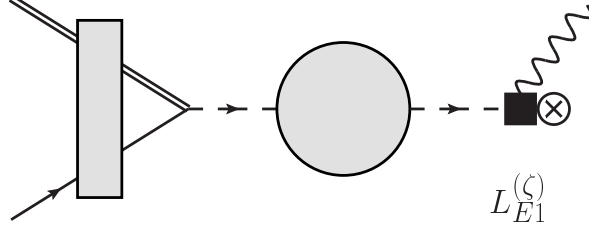


FIG. 5. Two-body current represented by the square. The rest of the notation is the same as in Figs 1, 2, 3.

The third contribution is from two-body currents in Eq. (6) that contribute to E1 capture to the ground and excited states. The diagram in Fig. 5 gives the contribution

$$\frac{2\pi C_0(\eta_p)e^{i\sigma_0} k_0}{-1/a_0 + \frac{r_0}{2}p^2 + \frac{s_0}{4}p^4 + \dots - 2k_C H(\eta_p)} \times L_{E1}^{(\zeta)}. \quad (38)$$

Thus we have the following expression for the capture amplitude from the initial  $s$ -wave state

$$\mathcal{A}(p)\Gamma_{aa}^{(\zeta)} \equiv -e^{i\sigma_0} C_0(\eta_p) \Gamma_{aa}^{(\zeta)} \left[ \frac{1}{\mu} A(p) + 1 - \frac{2\pi B^{(0)}(p) + \alpha_e B^{(1)}(p) + \Delta B(p) + \mu J_0(p)}{\mu^2 - \frac{1}{a_0} + \frac{r_0}{2}p^2 + \frac{s_0}{4}p^4 + \dots - 2k_C H(\eta_p)} - \frac{2\pi k_0}{-1/a_0 + \frac{r_0}{2}p^2 + \frac{s_0}{4}p^4 + \dots - 2k_C H(\eta_p)} \times L_{E1}^{(\zeta)} \right]. \quad (39)$$

The total cross section and the  $S$ -factor can be calculated as

$$\sigma(p) = \frac{1}{16\pi M^2} \frac{1}{2} \left[ \frac{p^2 + \gamma_1^2}{2\mu p} |M^{(2P_{1/2})}|^2 + \frac{p^2 + \gamma_0^2}{2\mu p} |M^{(2P_{3/2})}|^2 \right],$$

$$S_{34}(E) = E e^{2\pi\eta_p} \sigma(p = \sqrt{2\mu E}), \quad (40)$$

where we averaged over the initial  ${}^3\text{He}$  spin and summed over the final state photon polarization and  ${}^7\text{Be}$  spin. The amplitude squared is

$$|M^{(\zeta)}|^2 = (2j+1) \left( \frac{Z_\phi m_\psi}{M} - \frac{Z_\psi m_\phi}{M} \right)^2 \frac{64\pi\alpha_e M^2 ([h^{(\zeta)}]^2 \mathcal{Z}^{(\zeta)})}{\mu} \times [|\mathcal{A}(p)|^2 + 2|Y(p)|^2], \quad (41)$$

with angular momentum  $j = 1/2$  for the excited state and  $j = 3/2$  for the ground state. The function  $Y(p)$  is the contribution from  $d$ -wave initial states, Eq (30). These expressions reduce to the corresponding forms for the capture reaction  ${}^7\text{Li}(n, \gamma){}^8\text{Li}$  when the long-range Coulomb interaction is turned off [20, 21].

## VI. RESULTS AND ANALYSIS

To predict the  $S$ -factor at solar energies using the EFT expression in Eq. (40) we need to determine the elastic  $s$ - and  $p$ -wave scattering parameters, and the two couplings for two-body currents. Usually, one-body currents dominate. Thus we start the analysis with the diagrams from Figs. 3 and 4 that can be constrained by elastic scattering, in principle. However, the phase shifts for  ${}^3\text{He}(\alpha, \alpha){}^3\text{He}$  are poorly known. The phase shift analysis is from a very old source [37] that was analyzed again by Boykin *et al.* in Ref. [29] where the experimental errors were quantified.

Numerical analysis of the  $s$ -wave phase shifts yields  $a_0 \sim 20 - 30$  fm and  $r_0 \sim 1$  fm. The size of the effective range  $r_0$  is consistent with  $\Lambda \sim 1/r_0 \sim 150 - 200$  MeV which is about the pion mass, the expected breakdown scale of the halo EFT. We take the low-momentum scale  $Q$  to be about the binding momenta of the ground and excited states,  $\gamma_0 \sim \gamma_1 \sim 60 - 70$  MeV. Thus this suggests the scattering length to be fine-tuned. At an arbitrarily low momentum, the relative contribution of the diagrams from Fig. 4 compared to the diagrams in Fig. 3, see Eq. (39), is  $\sim 2\pi(B + \mu J_0)a_0/\mu^2$ . In the absence of Coulomb interaction  $2\pi(B + \mu J_0)/\mu^2 \sim Q$ . However, this naive expectation is invalidated due to the non-perturbative Coulomb contributions [14], and instead we find  $2\pi(B + \mu J_0)/\mu^2 \sim 1/a_0 \sim Q^3/\Lambda^2$ . Therefore the contribution from the second set of diagrams scales as  $\sim 2\pi(B + \mu J_0)a_0/\mu^2 \sim 1$  compared to the first set. This scaling holds over a range of momenta  $p \lesssim 70$  MeV.

The relative contribution of the two body currents scales as  $\sim a_0 k_0 L_{\text{E1}}^{(\zeta)}$ . The photon energy  $k_0$  scales as  $\sim Q^3/\Lambda^2$  since we count  $p/\mu \sim \gamma/\mu \sim Q/\mu \sim Q^2/\Lambda^2$  [14]. The relative contribution of the two body current is  $\sim a_0 Q^3 L_{\text{E1}}^{(\zeta)}/\Lambda^2 \sim L_{\text{E1}}^{(\zeta)}$  for  $a_0 \sim \Lambda^2/Q^3$ . For natural-size couplings  $L_{\text{E1}}^{(\zeta)} \sim 1$ , the two body currents also contribute at LO.

The NLO corrections to the capture amplitude come from the  $s$ -wave shape parameter corrections assuming  $s_0 \sim 1/\Lambda^3$ . The amplitude from Eq. (39) can now be expanded as

$$\begin{aligned} \mathcal{A}(p) &= \mathcal{A}_{\text{LO}}(p) + \mathcal{A}_{\text{NLO}}(p) + \dots, \\ \mathcal{A}_{\text{LO}}(p) &= e^{i\sigma_0} C_0(\eta_p) \left[ -\frac{A(p)}{\mu} - 1 + \frac{2\pi B^{(0)}(p) + \alpha_e B^{(1)}(p) + \Delta B(p) + \mu J_0(p) + \mu^2 k_0 L_{\text{E1}}^{(\zeta)}}{-\frac{1}{a_0} + \frac{r_0}{2} p^2 - 2k_C H(\eta_p)} \right], \\ \mathcal{A}_{\text{NLO}}(p) &= -e^{i\sigma_0} C_0(\eta_p) \frac{2\pi s_0 p^4}{\mu^2} \frac{B^{(0)}(p) + \alpha_e B^{(1)}(p) + \Delta B(p) + \mu J_0(p) + \mu^2 k_0 L_{\text{E1}}^{(\zeta)}}{4 \left[ -\frac{1}{a_0} + \frac{r_0}{2} p^2 - 2k_C H(\eta_p) \right]^2}. \end{aligned} \quad (42)$$

Naively,  $d$ -wave contributions would be NNLO, as they are suppressed by two relative

powers of momentum compared to capture from  $s$ -waves. In our fits this is confirmed at c.m. energies  $\lesssim 500$  keV ( $p \lesssim 30$  MeV). At higher energies ( $p \sim 60$  MeV)  $d$ -wave contributions are around  $\sim 25\%$ . This might be related to an accidental cancellation between the  $s$ -wave capture diagrams from Figs. 3 and 4 when  $a_0 \sim 30$  fm. We include the  $d$ -wave contribution in perturbation at NLO. Higher order two-body currents, and possible  $d$ -wave initial state strong interactions, would constitute NNLO errors.

We do a simultaneous fit to  $S$ -factor measurements and phase shift analysis to determine the parameters. At LO, the scattering parameters  $a_0$ ,  $r_0$ ,  $r_1^{(+)}$ ,  $r_1^{(-)}$  and two-body current couplings  $L_{E1}^{(+)}$  and  $L_{E1}^{(-)}$  describe the  $s$ -wave phase shift  $\delta_0$ ,  $p$ -wave phase shifts  $\delta_1^{(+)}$ ,  $\delta_1^{(-)}$  and the capture cross sections. At NLO, three additional scattering parameters  $s_0$ ,  $\sigma_1^{(+)}$ ,  $\sigma_1^{(-)}$  contribute to the respective phase shifts. Only  $s_0$  contributes to the capture process.

The capture data are from LUNA [38], Seattle [39], Weizmann [40], ERNA [41], and Notre Dame [42]. The  $S_{34}$  measurements include both prompt photon and activation data. For the former, the branching ratio  $R_0$  to the excited state compared to the ground state is available. The  $R_0$  data are useful as they remove normalization errors from the cross section measurements. We perform two sets of fits.

First, we fit the  $S_{34}$  and  $R_0$  to c.m. energies of about 500 keV. Though it would be preferable to fit the ERE parameters at low energies, the available phase shift data starts at around 1.9 MeV. For the  $p$ -wave, the binding momenta  $\gamma_0$  and  $\gamma_1$  provide a constraint at zero energy. For the  $s$ -wave, no such low-energy constraints exist. It leads to large errors in fitting  $a_0$ . At LO, we fit the phase shifts to about 2.5 MeV. At NLO, we increase the range of  $s$ -wave phase shift fit to about 3 MeV as we introduce the shape parameter  $s_0$ . We also use the LO value for  $r_0$  in the NLO fits. When we let  $r_0$  vary, we get similar values and fitting errors. However, the scattering length  $a_0$  and shape parameter  $s_0$  have large uncertainties though their central values are reasonable. Lack of low-energy phase shift information provides no meaningful constraints on  $a_0$ . We call this set of fits “Small range” in the plots. Second, we fit the  $S_{34}$  and  $R_0$  to c.m. energies of about 1000 keV, and all the elastic phase shifts to about 3 MeV. We call this the “Large range” fit in the plots. Again we keep  $r_0$  fixed to its LO value in the NLO fits. We also performed a Jackknife fit over the Large range, where we removed one whole data set from each of the five experimental groups LUNA, Seattle, Weizmann, ERNA and Notre Dame, in turn. This gave results very similar to the Large range.

Fits	$a_0$ (fm)	$r_0$ (fm)	$s_0$ (fm <sup>3</sup> )	$\rho_1^{(+)}$ (MeV)	$\sigma_1^{(+)}$ (fm)	$\rho_1^{(-)}$ (MeV)	$\sigma_1^{(-)}$ (fm)	$L_1^{(+)}$	$L_1^{(-)}$
Small range (LO)	$19.8 \pm 7.9$	$1.1 \pm 0.2$	—	$-55.4 \pm 0.8$	—	$-40.6 \pm 0.8$	—	$0.81 \pm 0.11$	$0.74 \pm 0.13$
Large range (LO)	$17.6 \pm 4.2$	$1.2 \pm 0.1$	—	$-56.1 \pm 0.4$	—	$-42.6 \pm 0.5$	—	$0.85 \pm 0.05$	$0.94 \pm 0.06$
Small range (NLO)	$24.8 \pm 4.7$	$1.1 \pm 0.2$	$-0.9 \pm 0.8$	$-57.8 \pm 1.7$	$1.68 \pm 0.07$	$-41.4 \pm 1.3$	$1.69 \pm 0.08$	$0.97 \pm 0.11$	$0.81 \pm 0.13$
Large range (NLO)	$21.6 \pm 3.4$	$1.2 \pm 0.1$	$-0.9 \pm 0.7$	$-55.4 \pm 0.5$	$1.59 \pm 0.03$	$-41.9 \pm 0.7$	$1.74 \pm 0.05$	$0.79 \pm 0.06$	$0.83 \pm 0.08$

TABLE I. EFT parameters. The parameters were determined from simultaneous fits to the capture  ${}^3\text{He}(\alpha, \gamma){}^7\text{Be}$ , and  ${}^3\text{He}(\alpha, \alpha){}^3\text{He}$  phase shift data as described in the text. We use the LO  $r_0$  values in the NLO fits.

In Table I, we summarize our fits. The parameters are self-consistent across the two different kinds of fits: Small range and Large range. This is reflected in the plots in Figs. 6, 7 and 8. The largest uncertainties were in the  $s$ -wave ERE parameters  $a_0$  and  $s_0$ . Within the uncertainties,  $a_0 \sim \Lambda^2/Q^3$ . The fitted  $s_0$  values were slightly smaller than the expected  $\sim 1/\Lambda^3$ . There is not a lot of difference in the LO and NLO capture cross sections at low energy, Fig. 6. This is consistent with a small  $s_0$ . The  $d$ -wave contributions are small, except at higher energies where they, still of size NLO, bring the EFT numbers in better agreement with capture data. Even the Small range numbers that were fitted to below 500 keV agrees with capture data around 1 MeV. The  $p$ -wave ERE parameters are consistent with the power-counting as well,  $\rho_1^{(\zeta)} \sim Q$ ,  $\sigma_1^{(\zeta)} \sim 1/\Lambda$ . The  $p$ -wave phase shifts are reproduced at NLO once the shape parameter  $\sigma_1^{(\zeta)}$  contributions are included, Fig 8. The dimensionless two-body current couplings are of natural size,  $L_{E1}^{(\zeta)} \sim \mathcal{O}(1)$ .

In Table II we list  $S_{34}(0)$  in EFT. The errors from the fits were propagated to the  $S$ -factor assuming a linear model as follows. For a function  $f(\mathbf{r}; \boldsymbol{\beta})$ , where  $\mathbf{r}$  is the independent variable and  $\boldsymbol{\beta}$  the parameter set, we estimate the error as

$$\delta f(\mathbf{r}; \boldsymbol{\beta}) = \sqrt{\frac{\partial f(\mathbf{r}; \boldsymbol{\beta})}{\partial \beta_i} \text{COV}_{ij} \frac{\partial f(\mathbf{r}; \boldsymbol{\beta})}{\partial \beta_j}}, \quad (43)$$

where  $\text{COV}_{ij}$  are the elements of the covariance matrix. We indicate a theory error of 30% and 10%, respectively, in our LO and NLO estimates. The central values of the EFT fits are compatible within the errors with other estimates (0.593 keV b from FMD [43], 0.59 keV b from NCSM [44],  $(0.567 \pm 0.018 \pm 0.004)$  keV b from LUNA [38],  $(0.595 \pm 0.018)$  keV b from Seattle [39],  $(0.53 \pm 0.02 \pm 0.01)$  keV b from Weizmann [40],  $(0.57 \pm 0.04)$  keV b from ERNA [41], and  $(0.554 \pm 0.020)$  keV b from Notre Dame [42]).

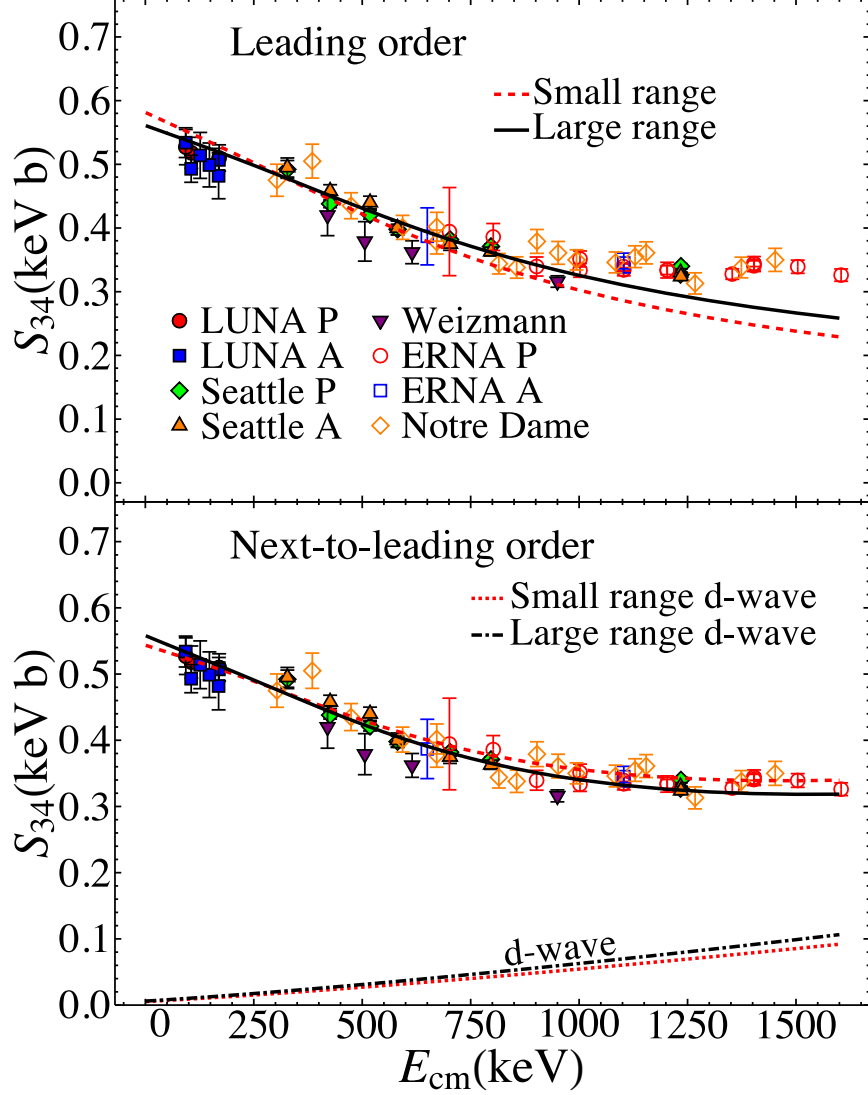


FIG. 6.  $S$ -factor  $S_{34}$  for c.m. energy  $E_{cm}$  at LO (top panel) and NLO (bottom panel). The capture data are from LUNA [38], Seattle [39], Weizmann [40], ERNA [41], and Notre Dame [42]. The letters P and A after the experiment name are used to distinguish between prompt and activation data as appropriate. The red dashed, and black solid curves are the halo EFT results from two different fits described in the text. We show the  $d$ -wave contributions at NLO as red dot and black dot-dashed curves in the bottom panel for the two different fits.

Finally, we comment on potential model calculations that do not include the two-body current contributions. As mentioned, there is a large cancellation between the diagrams from Figs. 3 and 4. In the absence of two-body currents this would require the wave function renormalization constant to be large. This, however, is not an issue since a small variation

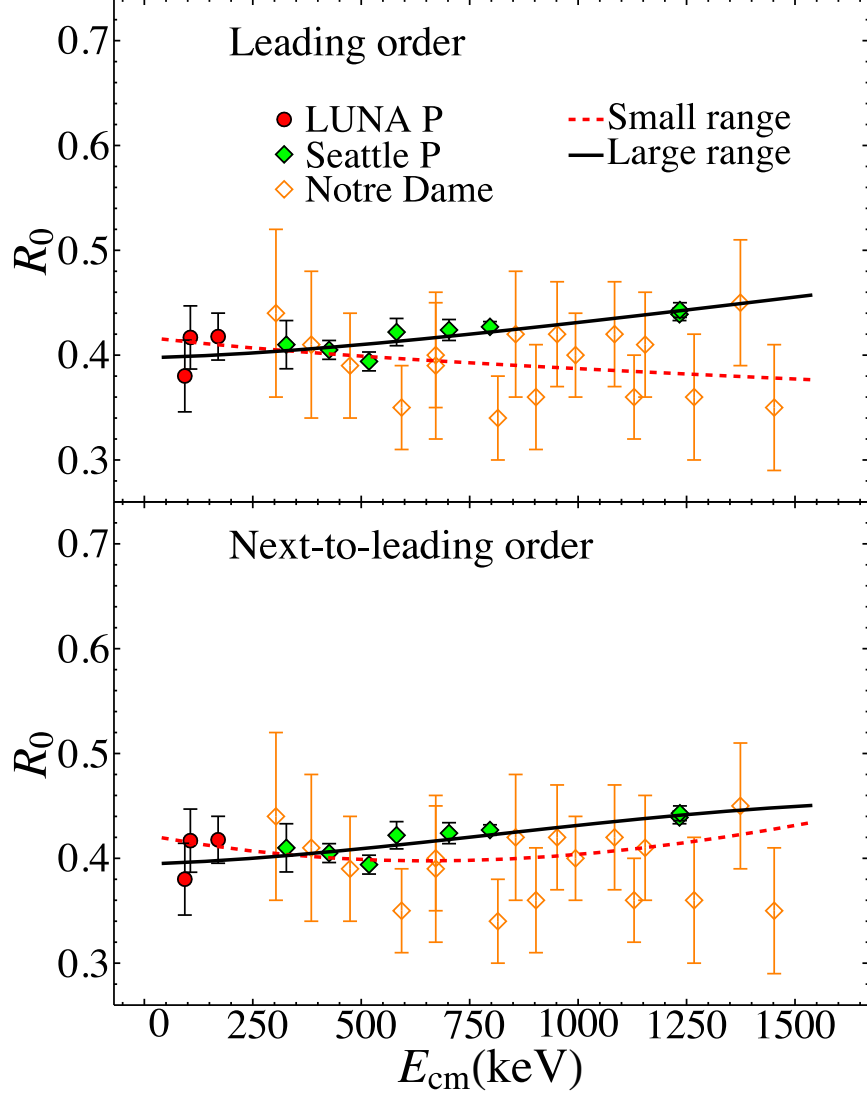


FIG. 7. Branching ratio  $R_0$  for capture to excited state to ground state for  ${}^3\text{He}(\alpha, \gamma){}^7\text{Be}$  at LO (top panel) and NLO (bottom panel). Data are from LUNA [38], Seattle [39], and Notre Dame [42]. The rest of the notation is the same as Fig. 6.

in  $\rho_1^{(\zeta)}$  can cause the normalization constant to be huge.  $[h^{(+)}]^2 \mathcal{Z}^{(+)}$  and  $[h^{(-)}]^2 \mathcal{Z}^{(-)}$  have a pole at approximately  $\rho_1^{(+)} = -47.4$  MeV and  $\rho_1^{(-)} = -32.4$  MeV, respectively, see Eq (28). We explore this idea in Fig. 9 where  $d$ -wave contributions were not included to highlight the cancellation. For illustration we fit the prompt data from LUNA [38], Seattle [39], and Notre Dame [42] with and without the two-body current, to about 1200 keV. We also include some phase shift data. The results are similar. The curve without two-body currents used  $\rho_1^{(+)} \approx -49$  MeV and  $\rho_1^{(-)} \approx -36$  MeV, which are only slightly different than those in

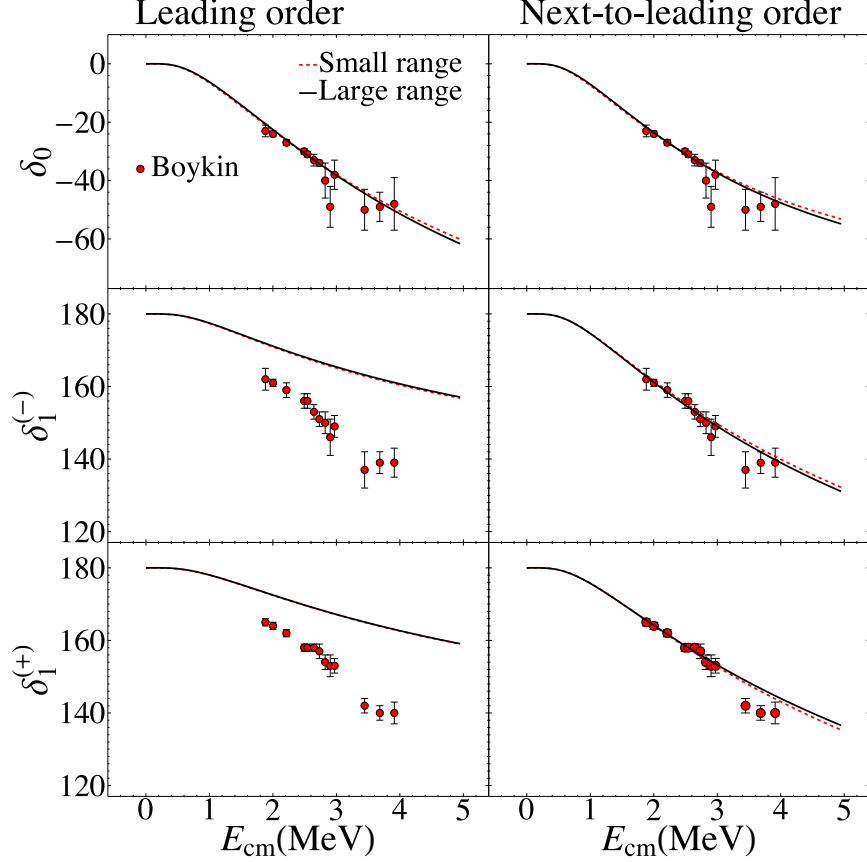


FIG. 8.  ${}^3\text{He}-\alpha$  scattering phase shifts at LO (left panel) and NLO (right panel), as functions of the c.m. energy  $E_{\text{cm}}$ . The data is from Ref. [29]. The rest of the notation is the same as Fig. 6.

Table I but lead to much larger wave function renormalization constant. The asymptotic normalization constants (ANC) were evaluated in potential models, see Ref. [45]. These are related to the wave function renormalization we calculate via

$$C_{1, \zeta}^2 = \frac{[\gamma^{(\zeta)}]^2 \Gamma(2 + k_C/\gamma^{(\zeta)})}{\pi} [h^{(\zeta)}]^2 \mathcal{Z}^{(\zeta)}. \quad (44)$$

Using the calculated ANCs [45]  $C_{1,2P_{3/2}}^2 = 23.3 \text{ fm}^{-1}$  and  $C_{1,2P_{1/2}}^2 = 15.9 \text{ fm}^{-1}$ , we get  $\rho_1^{(+)} = -52.3 \text{ MeV}$  and  $\rho_1^{(-)} = -38.7 \text{ MeV}$ , respectively, in quite good agreement with the EFT numbers without two-body currents.

## VII. CONCLUSIONS

The capture cross section  $\sigma$  and the related  $S$ -factor  $S_{34}$  for  ${}^3\text{He}(\alpha, \gamma){}^7\text{Be}$  were calculated at low energies in halo EFT. E1 transitions from initial  $s$ - and  $d$ -wave states to the bound

Fit	$S_{34}(0)$ (keV b)
Small range LO	$0.582 \pm 0.011$ (fit) $\pm 0.194$ (EFT)
Large range LO	$0.561 \pm 0.007$ (fit) $\pm 0.187$ (EFT)
Small range NLO	$0.544 \pm 0.012$ (fit) $\pm 0.054$ (EFT)
Large range NLO	$0.558 \pm 0.008$ (fit) $\pm 0.056$ (EFT)

TABLE II.  $S_{34}$  at threshold. In the EFT results, the first error estimate is from the fits and the second is an estimated 30% and 10% error to the LO and NLO EFT results, respectively. Note that the EFT results are evaluated at  $E = 20 \times 10^{-3}$  keV.

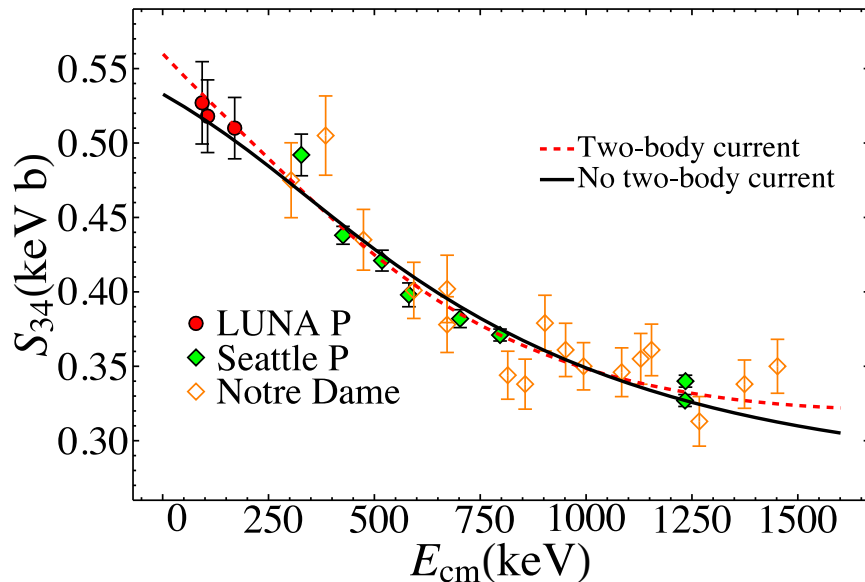


FIG. 9.  $S_{34}$  as a function of the c.m. energy  $E_{cm}$ . The fits include only prompt data from LUNA [38], Seattle [39], and Notre Dame [42], with (red-dashed) and without (blue-solid) the two-body currents, to about 1200 keV.

$p$ -wave ground and excited states were considered. The Coulomb photons between the two clusters  ${}^3\text{He}$  and  $\alpha$  were iterated to all orders in perturbation. The LO contributions to E1 transitions come from the initial  $s$ -wave Coulomb and short-range interactions, and from two-body currents. At NLO,  $s$ -wave shape parameter and pure Coulomb  $d$ -wave initial state interactions were included.

We determine the low-energy parameters by a simultaneous fit of the halo EFT expres-

sions to  $S_{34}$  measurements, and  $s$ - and  $p$ -wave phase shifts. Two different fits were employed that gave very similar results. The fits corroborate the adopted power-counting where the  $s$ -wave scattering length and effective range both contribute at LO. The contribution from the  $s$ -wave shape parameter is suppressed by a factor of  $Q/\Lambda$  compared to LO. Pure Coulomb  $d$ -wave initial state interactions do not contribute significantly ( $\lesssim 10\%$ ) up to  $E_{\text{cm}} \sim 500$  keV, and above that it behaves like a typical ( $\lesssim 30\%$ ) NLO correction. We estimate a 10% error in the EFT results from higher order NNLO contributions from initial state  $d$ -wave strong interactions and higher order two-body currents.

Despite the apparently good description of data, reasonable agreement among the different fit schemes, and a converging pattern from LO to NLO, our fits use elastic scattering data mostly concentrated on the high-energy end of the validity range of the halo EFT. That causes certain instabilities in finding the optimal set of fitting parameters, since they should in principle be better fixed at lower energies where data are scarce or even non-existent. Nevertheless the halo EFT results for  $S_{34}(0)$  are in good agreement with some model extrapolations of experimental measurements [38–42] and also recent ab initio calculations [43, 44].

Moreover, we find with the current dataset that the contribution of two-body currents is strongly correlated to the wave function renormalization constants in a way that a decrease in one is compensated by an increase in the other. We showed the possibility of fitting phase shifts and capture data to our expressions without two-body currents, similar to what is done in potential model calculations. Experimental phase shifts at lower energies are likely to provide stronger constraints on the EFT parameters with great chance to disentangle the role of these terms. The planned TRIUMF experiment to measure phase shifts down to c.m. energies of about 500 keV [46] would be useful to constrain the low-energy theory. It would determine the wave function renormalization constants directly from elastic scattering data without resorting to fits to capture data. The expressions presented here can be directly applied to  ${}^3\text{H}(\alpha, \gamma){}^7\text{Li}$  capture calculation where the main difference is the charge  $Z_\psi = 1$  of the  ${}^3\text{H}$  nucleus. The EFT parameters would have to be tuned to the  ${}^3\text{H}\text{-}\alpha$  system. This work is under progress.

## ACKNOWLEDGMENTS

The authors thank D. R. Phillips and X. Zhang for pointing out a mistake in one of our expressions, and other comments on the manuscript. G.R. thanks the Institute of Physics at University of São Paulo, the Institute for Nuclear Theory at University of Washington, the Kavli Institute of Theoretical Physics at University of California Santa Barbara, for kind hospitality during part of the completion of this research. G.R. acknowledges partial support from the Joint Institute for Nuclear Physics and Applications at Oak Ridge National Laboratory and the Department of Physics, University of Tennessee during his sabbatical where part of this research was completed. This work was partially supported by U.S. NSF grants PHY-1307453, PHY-1615092, Brazilian agency FAPESP-2012/50984-4, and Brazilian project INCT-FNA Proc. No. 464898/2014-5.

- 
- [1] R. H. Cyburt and B. Davids, *Phys. Rev.* **C78**, 064614 (2008).
  - [2] J. N. Bahcall and R. K. Ulrich, *Rev. Mod. Phys.* **60**, 297 (1988).
  - [3] E. G. Adelberger *et al.*, *Rev. Mod. Phys.* **70**, 1265 (1998).
  - [4] S. Fukuda *et al.* (Super-Kamiokande), *Phys. Rev. Lett.* **86**, 5651 (2001).
  - [5] B. Aharmim *et al.* (SNO), *Phys. Rev.* **C75**, 045502 (2007).
  - [6] J. N. Bahcall and A. M. Serenelli, *Astrophys. J.* **626**, 530 (2005).
  - [7] J. N. Bahcall, A. M. Serenelli, and S. Basu, *Astrophys. J.* **621**, L85 (2005).
  - [8] C. Arpesella *et al.* (Borexino), *Phys. Rev. Lett.* **101**, 091302 (2008).
  - [9] R. H. Cyburt, *Phys. Rev.* **D70**, 023505 (2004).
  - [10] B. D. Fields, *Ann. Rev. Nucl. Part. Sci.* **61**, 47 (2011).
  - [11] E. G. Adelberger *et al.*, *Rev. Mod. Phys.* **83**, 195 (2011).
  - [12] C. A. Bertulani, H. W. Hammer, and U. van Kolck, *Nucl. Phys.* **A712**, 37 (2002).
  - [13] P. F. Bedaque, H. W. Hammer, and U. van Kolck, *Phys. Lett.* **B569**, 159 (2003).
  - [14] R. Higa, H.-W. Hammer, and U. van Kolck, *Nucl.Phys.* **A809**, 171 (2008).
  - [15] B. A. Gelman, *Phys.Rev.* **C80**, 034005 (2009).
  - [16] D. L. Canham and H.-W. Hammer, *Eur.Phys.J.* **A37**, 367 (2008), 0807.3258.
  - [17] D. L. Canham and H.-W. Hammer, *Nucl.Phys.* **A836**, 275 (2010), 0911.3238.

- [18] V. Lensky and M. C. Birse, Eur.Phys.J. **A47**, 142 (2011).
- [19] H.-W. Hammer and D. Phillips, Nucl.Phys. **A865**, 17 (2011).
- [20] G. Rupak and R. Higa, Phys.Rev.Lett. **106**, 222501 (2011).
- [21] L. Fernando, R. Higa, and G. Rupak, Eur. Phys. J. **A48**, 24 (2012).
- [22] G. Rupak, L. Fernando, and A. Vaghani, Phys. Rev. **C86**, 044608 (2012).
- [23] X. Zhang, K. M. Nollett, and D. R. Phillips, Phys. Rev. **C89**, 024613 (2014).
- [24] X. Zhang, K. M. Nollett, and D. R. Phillips, Phys. Rev. **C89**, 051602 (2014).
- [25] E. Ryberg, F. Christian, H. W. Hammer, and L. Platter, Eur. Phys. J. **A50**, 170 (2014).
- [26] X. Zhang, K. M. Nollett, and D. R. Phillips, Phys. Lett. **B751**, 535 (2015).
- [27] G. Rupak, Int. J. Mod. Phys. **E25**, 1641004 (2016).
- [28] TUNL Nuclear Data Evaluation Project, “*Energy Level Diagram,  ${}^7\text{Be}$  (2002)*”. Available at [http://www.tunl.duke.edu/nucldata/figures/07figs/07\\_04\\_2002.pdf](http://www.tunl.duke.edu/nucldata/figures/07figs/07_04_2002.pdf).
- [29] W. R. Boykin, S. D. Baker, and D. M. Hardy, Nucl. Phys. A **195**, 241 (1972).
- [30] S. R. Beane and M. J. Savage, Nucl. Phys. **A694**, 511 (2001).
- [31] J. Carlson, D. O. Riska, R. Schiavilla, and R. B. Wiringa, Phys. Rev. **C42**, 830 (1990).
- [32] J. Carlson, D. O. Riska, R. Schiavilla, and R. B. Wiringa, Phys. Rev. **C44**, 619 (1991).
- [33] H. Sadeghi, R. Ghasemi, and H. Khalili, Chin. Phys. **C38**, 084101 (2014), [Astrophys. Space Sci.347,261(2013)].
- [34] M. Abramowitz and I. A. Stegun, eds., *Handbook of mathematical functions : with formulas, graphs, and mathematical tables* (Dover, New York, 1965).
- [35] I. J. Thompson, NIST Digital Library of Mathematical Functions, “*Chapter 33: Coulomb Functions*”, <http://dlmf.nist.gov/33>.
- [36] D. B. Kaplan, M. J. Savage, and M. B. Wise, Phys. Lett. **B424**, 390 (1998).
- [37] R. J. Springer and T. A. Tombrello, Phys. Rev. **163**, 964 (1967).
- [38] H. Constantini *et al.*, Nucl. Phys. A **814**, 144 (2008).
- [39] T. A. D. Brown *et al.*, Phys. Rev. C **76**, 055801 (2007).
- [40] B. S. Nara Singh, M. Hass, Y. Nir-El, and G. Haquin, Phys. Rev. Lett. **93**, 262503 (2004).
- [41] A. Di Leva *et al.*, Phys. Rev. Lett **102**, 232502 (2009).
- [42] A. Kontos, E. Uberseder, R. deBoer, J. Grres, C. Akers, A. Best, M. Couder, and M. Wiescher, Phys. Rev. **C87**, 065804 (2013), [Addendum: Phys. Rev.C88,no.1,019906(2013)].
- [43] T. Neff, Phys. Rev. Lett. **106**, 042502 (2011).

- [44] J. Dohet-Eraly *et al.*, Phys. Lett. **B757**, 430 (2016).
- [45] S. B. Igamov, K. I. Tursunmakhatov, and R. Yarmukhamedov, Phys. Rev. **C85**, 045807 (2012).
- [46] B. Davids, “Elastic scattering of  ${}^3\text{He}+\alpha$  with SONIK,” (2016), private communication.